Monthly Notices of the ROYAL ASTRONOMICAL SOCIETY

MNRAS **522,** 3049–3057 (2023) https://doi.org/10.1093/mnras/stad1109
Advance Access publication 2023 April 17

Reaction dynamics of $C(^3P) + Si_2(X\ ^3\Sigma_g^-) \rightarrow Si(^3P) + SiC(X\ ^3\Pi)$ on a global CHIPR potential energy surface of the ground state $Si_2C(X\ ^1A_1)$

Ximing Li,[1,2] Zhi Qin [1,2]★ Guangan Chen[1,2] and Linhua Liu [1,2,3]★

[1]*School of Energy and Power Engineering, Shandong University, Jinan 250061, China*
[2]*Optics and Thermal Radiation Research Center, Institute of Frontier and Interdisciplinary Science, Shandong University, Qingdao, Shandong 266237, China*
[3]*School of Energy Science and Engineering, Harbin Institute of Technology, Harbin 150001, China*

Accepted 2023 April 11. Received 2023 April 7; in original form 2023 March 9

ABSTRACT

The dynamics of $C(^3P) + Si_2(X\ ^3\Sigma_g^-) \rightarrow Si(^3P) + SiC(X\ ^3\Pi)$ on its ground state $Si_2C(X\ ^1A_1)$ are of great significance in carbon-rich interstellar chemistry. Using the combined-hyperbolic-inverse-power-representation method, we construct the first global potential energy surface (PES) for the electronic ground state $Si_2C(X\ ^1A_1)$ based on a total of 4080 *ab initio* energy points, which are obtained at the Davidson-corrected internally contracted multireference configuration interaction level of theory. The topographical features of the newly constructed PES are examined in detail and show good agreement with previous theoretical and experimental studies. Finally, we investigate the $C(^3P) + Si_2(X\ ^3\Sigma_g^-) \rightarrow Si(^3P) + SiC(X\ ^3\Pi)$ reaction using the quasi-classical trajectory and time-dependent wave packet calculations, yielding reasonable integral cross sections and rate constants, which are expected to be useful for astrochemical modelling in carbon-rich interstellar environments.

Key words: (*ISM*:) dust, extinction – astrochemistry – molecular processes.

1 INTRODUCTION

The interstellar dust, consisting of carbon and silicon, is the intellectual driver for studying the physics and chemistry of the carbon-rich asymptotic giant branch (AGB) stars (Frenklach, Carmer & Feigelson 1989; Gobrecht et al. 2017; McCarthy, Gottlieb & Cernicharo 2019). As the simplest diatomic molecule composed solely of the silicon and carbon atoms, SiC is believed to be an important component in the chemical evolution of the carbon-star IRC+10216 (Cernicharo et al. 1989, 2018; Witsch et al. 2019). Although several efforts have been devoted to understand the reaction processes involved SiC chemistry, including the dissociative recombination (Prasad & Huntress 1980; Zhu et al. 2022), neutral–neutral interaction (Smith, Herbst & Chang 2004), and photodissociation (McElroy et al. 2013), many possible reaction paths are still poorly understood.

The disilicon carbon (Si_2C), one of the prominent species in the carbon-rich stars such as IRC+10216 (Cernicharo et al. 2015, 2018), is thought to be an important constituent of the interstellar dust. Si_2C is involved in the chemistry of evolved carbon-rich stars and plays an important role in molecular astronomy (Mauron & Huggins 2000; Cordiner & Millar 2009; McCarthy et al. 2015). The mass spectrometric studies (Verhaegen, Stafford & Drowart 1964; Schmude & Gingerich 1997; Pellarin et al. 1999) also indicate it is the common gas-phase polyatomic fragment in the evaporation of bulk silicon carbide below about 2000 K, which provides indirect evidence for the importance of Si_2C. In addition, Si_2C is thought to be an important intermediate in the production of SiC dust grains (Cernicharo et al. 2015). Hence, the study of the ground state $Si_2C(X\ ^1A_1)$ system and its associated reaction of $C(^3P) + Si_2(X\ ^3\Sigma_g^-) \rightarrow Si(^3P) + SiC(X\ ^3\Pi)$ can be helpful to characterize the chemical evolution for the formation of SiC dust grains in interstellar space.

Previous experimental studies mainly focused on the structure and spectrum of the ground state $Si_2C(X\ ^1A_1)$. The spectrum of Si_2C was first tentatively identified by Weltner & McLeod (1964) in the numerous molecules vapourizing from silicon carbide. Then, Kafafi et al. (1983) reported the infrared spectra of $Si_2^{12}C$ and $Si_2^{13}C$ in the 400 – 4000 cm^{-1} and concluded that the molecule had a C_{2v} equilibrium structure. Presilla-Márquez & Graham (1991) recorded the spectra of Si_2C and assigned the symmetric (υ_1), bending (υ_2), and antisymmetric (υ_3) modes of Si_2C to 839.5, 166, and 1188.4 cm^{-1}, respectively. Later, Cernicharo et al. (2015) reported the discovery of Si_2C in interstellar space in 2015. In the same year, Steglich & Maier (2015) reported the UV- and optical gas-phase spectrum of Si_2C for the first time. Subsequently, Reilly et al. (2015) investigated the ground state rovibrational structure of Si_2C using mass-resolved and fluorescence spectroscopy and variational calculations performed on a high-level *ab initio* potential energy surface (PES). They derived the barrier to the linearity of 783(48) cm^{-1} from the Dixon-dip plot of the Si_2C bending wavenumbers with the value in parentheses being an estimated uncertainty. They also determined the experimental υ_1 and υ_2 fundamental frequencies of 832 and 142 cm^{-1}, respectively, and the computational υ_3 fundamental band of 1198 cm^{-1}. McCarthy et al. (2015) investigated the rotational spectrum using sensitive microwave techniques aided by high-level *ab initio* methods and accurately determined the equilibrium structure using isotopic substitution and vibrational corrections. The C_{2v} equilibrium structure of Si_2C was shown to be the Si–C bond length of 1.693 Å and ∠[Si–C–Si] of 114.87°. In 2018, Cernicharo et al. (2018) observed 30 additional rotational lines of Si_2C towards IRC+10216. Later,

★ E-mail: z.qin@sdu.edu.cn (ZQ); liulinhua@sdu.edu.cn (LL)

Witsch et al. (2019) studied the υ_3 antisymmetric stretching mode of Si_2C using a narrow line width infrared quantum cascade laser spectrometer and determined υ_3 of Si_2C at 1202.21 cm^{-1}.

Theoretically, several studies were done to calculate the equilibrium geometry and spectrum of Si_2C (Diercksen et al. 1985; Grev & Schaefer 1985; So 1985; Sabin et al. 1986; Largo-Cabrerizo & Flores 1988; Rittby 1991; Bolton et al. 1992). In particular, Grev & Schaefer (1985) calculated the equilibrium geometry of the ground state Si_2C at the self-consistent-field (SCF) level of theory with a double zeta plus polarization basis set and showed that the global minimum (GM) structure located at 2.1 kcal mol^{-1} below the $D_{\infty h}$ transition state. Rittby (1991) investigated the ground state Si_2C using various basis sets at the Hartree–Fock level and many-body perturbation theory to second order. Vibrational frequencies, infrared intensities, and isotopic shifts were also presented and agreed well with previous theoretical investigations (Diercksen et al. 1985; Grev & Schaefer 1985; So 1985; Sabin et al. 1986; Largo-Cabrerizo & Flores 1988). Sharma & Chandra (2022) solved a set of 200 statistical equilibrium equations coupled with 867 radiative transfer equations of para-Si_2C. Their obtained transitions can play important role in the identification of Si_2C in the cosmic objects. However, the above-mentioned studies have not covered the analytical PES for the ground state of Si_2C.

The analytical PES for $Si_2C(X\ ^1A_1)$ was reported by several attempts (Barone, Jensen & Minichino 1992; Gabriel et al. 1992; Spielfiedel et al. 1996; Reilly et al. 2015; Koput 2017). (Barone et al. 1992) computed *ab initio* potential energy points by the MP2 method using a large basis set including *f* functions and fitted them to an internal-coordinate polynomial function up to the fourth degree. Their calculated vibrational frequencies are compared well with the experimental values of Presilla-Márquez & Graham (1991). Gabriel et al. (1992) reported a PES for the ground state of Si_2C obtained from multireference configuration interaction (MRCI) calculations and used it to evaluate the vibration-rotation energy levels. Their PES determined the height of the barrier to linearity to be 310 cm^{-1}. Spielfiedel et al. (1996) constructed different potential energy functions of the ground state and electronically excited singlet and triplet states of Si_2C using *ab initio* potential energy points from different levels of theory. The potential energy function of the ground state Si_2C yielded a barrier to the linearity of 859 cm^{-1}. Recently, Koput (2017) reported an analytical PES for the ground state Si_2C using *ab initio* potential energy points obtained by the coupled-cluster calculations, in which the core-electron correlation, high-order valence-electron correlation, scalar relativistic, and adiabatic effects were considered. Based on this PES, the υ_1, υ_2, and υ_3 were predicted to be 832.8, 140.1, and 1203.6 cm^{-1}, respectively, and the υ_2 was reproduced to the experimental uncertainty of ± 2 cm^{-1}.

All analytical PESs mentioned earlier only focused on the specific geometries near the equilibrium regions for the electronic states of the Si_2C and were mainly concerned with energy, equilibrium geometry, and vibrational frequencies. However, an analytically global PES can exhibit detailed topographical features, including the dissociation limits and barriers on the entrance channel, which are the key to studying the reaction dynamics of the $Si_2C(X\ ^1A_1)$ system. Due to the lack of the global PES for $Si_2C(X\ ^1A_1)$, its associated dynamics have not been studied yet. In this work, we aim to construct a global PES of the ground state $Si_2C(X\ ^1A_1)$ and carry out a tentative study of the dynamics of the $C(^3P) + Si_2(X\ ^3\Sigma_g^-) \rightarrow Si(^3P) + SiC(X\ ^3\Pi)$ reaction. All *ab initio* potential energy points of the $Si_2C(X\ ^1A_1)$ system were calculated at the MRCI (Knowles & Werner 1988; Werner & Knowles 1988) level of theory with the Davidson correction (+ Q). The potential energy points were then employed to construct the PES using the combined-hyperbolic-inverse-power-representation (CHIPR) method (Varandas 2013, 2014; Rocha & Varandas 2020, 2021), which was widely used in previous studies (Chen et al. 2022; Li et al. 2022; Rocha, Linnartz & Varandas 2022; Ding, Qin & Liu 2023). The rms deviation (rmsd) of this novel PES from the *ab initio* results is 0.769 kcal mol^{-1}. For a better understanding of the $C(^3P) + Si_2(X\ ^3\Sigma_g^-) \rightarrow Si(^3P) + SiC(X\ ^3\Pi)$ reaction, the quasi-classical trajectory (QCT) and quantum mechanical (QM) methods were both employed to compute the integral cross sections (ICSs) and rate constants based on the obtained CHIPR $Si_2C(X\ ^1A_1)$ PES.

This work is organized as follows: Section 2 presents the details of the *ab initio* calculations for $Si_2C(X\ ^1A_1)$. The CHIPR method for fitting the $Si_2C(X\ ^1A_1)$ PES is described in Section 3. Section 4 discusses the topographical characteristics of the $Si_2C(X\ ^1A_1)$ PES. The QCT and QM dynamic calculations for $C(^3P) + Si_2(X\ ^3\Sigma_g^-) \rightarrow Si(^3P) + SiC(X\ ^3\Pi)$ reaction are given in Section 5. Finally, conclusions are drawn in Section 6.

2 *AB INITIO* CALCULATIONS

In this work, *ab initio* calculations were performed with the MOLPRO 2015 package (Werner et al. 2015, 2020). The *ab initio* energy points for mapping the PES were computed at the MRCI (Knowles & Werner 1988; Werner & Knowles 1988) level of theory with the Davidson correction [MRCI(Q)] based on the complete active space self-consistent field (CASSCF) (Knowles & Werner 1985; Werner & Knowles 1985) wave function. 12 electrons in the outermost shell were put into the active space distributed among twelve orbitals ($9a' + 3a''$). The Dunning's correlation consistent quadruple-zeta basis augmented by diffuse functions, aug-cc-pV(Q+d)Z [AV(Q + d)Z] (Dunning 1989) and aug-cc-pVQZ (AVQZ) were employed for the Si and C atoms, respectively. Our calculations of potential energies were based on a finite basis set, the complete basis set (CBS) extrapolation method may enhance the accuracy as suggested in previous studies (Varandas 2018a, b). A total of 4080 grid points were defined in Jacobi coordinates (R, r, and θ). For the C + Si_2 channel, the grids were set as $4.2 \leq r_{Si\text{-}Si}/a_0 \leq 6.0$, $1.0 \leq R_{C\text{-}SiSi}/a_0 \leq 15.0$, and $0 \leq \theta/\mathrm{deg} \leq 180.0$. For the Si + SiC channel, the ranges were defined by $3.0 \leq r_{C\text{-}Si}/a_0 \leq 6.0$, $1.5 \leq R_{Si\text{-}SiC}/a_0 \leq 15.0$, and $0 \leq \theta/\mathrm{deg} \leq 180.0$. In addition, *ab initio* potential energy points of the $Si_2(X\ ^3\Sigma_g^-)$) and $SiC(X\ ^3\Pi)$ were calculated using the same level of theory and basis sets as $Si_2C(X\ ^1A_1)$.

3 THE CHIPR PES

According to the spin-spatial Wigner–Witmer correlation rules, the dissociation scheme for the ground state $Si_2C(X\ ^1A_1)$ can be described as follows:

$$Si_2C(X\ ^1A_1) \rightarrow \begin{cases} C(^3P) + Si_2(X\ ^3\Sigma_g^-) \\ Si(^3P) + CSi(X\ ^3\Pi) \\ C(^3P) + Si(^3P) + Si(^3P) \end{cases} \quad (1)$$

According to the CHIPR method (Varandas 2013, 2014; Rocha & Varandas 2020, 2021), the global PES of $Si_2C(X\ ^1A_1)$ assumes the following many-body expansion (MBE) form (Murrell et al. 1984)

$$V_{\mathrm{tot}}(R_1, R_2, R_3) = \sum_{i=1}^{3} V_i^{(1)} + V_{Si_1Si_2}^{(2)}(R_1) + V_{CSi_1}^{(2)}(R_2) + V_{CSi_2}^{(2)}(R_3) + V_{Si_2C}^{(3)}(R_1, R_2, R_3), \quad (2)$$

where V_{tot} is the calculated MRCI(Q) potential energy for any geometry of Si_2C, $V^{(1)}$ is the one-body energy of each atom, $V^{(2)}$ are the two-body (diatomic) potential energies of $Si_2(X\,^3\Sigma_g^-)$ and $SiC(X\,^3\Pi)$ corresponding to two dissociation schemes, and $V^{(3)}$ is the three-body term. As the zero-point of the potential energy corresponds to the three isolated ground-state atoms, the $V^{(1)}$ equals zero.

The CHIPR n-body term (n $\geq$ 2) assumes the following form (Varandas 2014; Rocha & Varandas 2020, 2021):

$$V^{(n)} = \sum_{\substack{i_1=0,\ldots \\ i_\tau=0}}^{L} C_{i_1,\ldots,i_\tau} \left[\prod_{p=1}^{\tau} y_p^{i_p}\right], \tag{3}$$

where $C_{i_1,\cdots,i_\tau}$ is the expansion coefficient of the Lth-order polynomial, y_p is the basis set of $p = 1, 2, \ldots, \tau$ (τ is the number of internal degrees of freedom for the n-atom molecule) coordinate for the reference geometry, and can be expanded in terms of the distributed-origin contracted basis sets (Varandas 2014; Rocha & Varandas 2020, 2021):

$$y_p = \sum_{\alpha=1}^{M-1} c_\alpha \phi_{p,\alpha} + c_M \phi_{p,M}, \tag{4}$$

where c_α and c_M are contraction coefficients and α denotes each primitive function $\phi_{p,\alpha}$. The primitive functions $\phi_{p,\alpha}$ and $\phi_{p,M}$ assume the forms as follows:

$$\phi_{p,\alpha} = \mathrm{sech}^{\eta_\alpha}\left[\gamma_{p,\alpha}\left(R_p - R_{p,\alpha}^{\mathrm{ref}}\right)\right] \tag{5}$$

$$\phi_{p,M} = \left[\frac{\tanh\left(0.2R_p\right)}{R_p}\right]^6 \mathrm{sech}\left[\gamma_{p,M}\left(R_p - R_{p,\alpha}^{\mathrm{ref}}\right)\right], \tag{6}$$

where $\gamma_{p,\alpha}$ and $\gamma_{p,M}$ are non-linear parameters. It is noted that equation (5) is used when ignoring the long-range terms. Otherwise, equation (6) should be utilized. Here, both primitive functions are used in equation (4). The $R_p - R_\alpha^{\mathrm{ref}}$ means the deviation of the coordinate R_p from the primitive origin R_α^{ref}, and the distributed origin R_α^{ref} assumes the following form:

$$R_{p,\alpha}^{\mathrm{ref}} = \zeta\left(R_p^{\mathrm{ref}}\right)^{\alpha-1}, \tag{7}$$

where ζ and R_p^{ref} are two constants that should be chosen reasonably during the fitting.

In equation (2), the CHIPR two-body terms are given by

$$V^{(2)}(R) = \frac{Z_A Z_B}{R}\sum_{k=1}^{L} C_k y^k, \tag{8}$$

where Z_A and Z_B represent the nuclear charges of A and B, respectively. C_k is the coefficient of the Lth-order polynomial. In addition, the three-body term in equation (2) assumes the form (Rocha & Varandas 2020, 2021):

$$V^{(3)} = \sum_{i,j,k=0}^{L} C_{i,j,k}\left\{\sum_{g\in G}^{} \mathcal{P}_g^{(i,j,k)}\left[y_1^i y_2^j y_3^k\right]\right\}, \tag{9}$$

where $C_{i,j,k}$ is the expansion coefficient, y_p ($p = 1, 2, 3$; 1 for Si_2, 2, 3 for SiC, respectively) has the form of equation (4) and $\mathcal{P}_g^{(i,j,k)}$ is the operator that reflects the permutation symmetry of atoms in a subgroup G of the S_3 symmetric group. Further details of the CHIPR method are fully described in previous studies (Rocha & Varandas 2020, 2021).

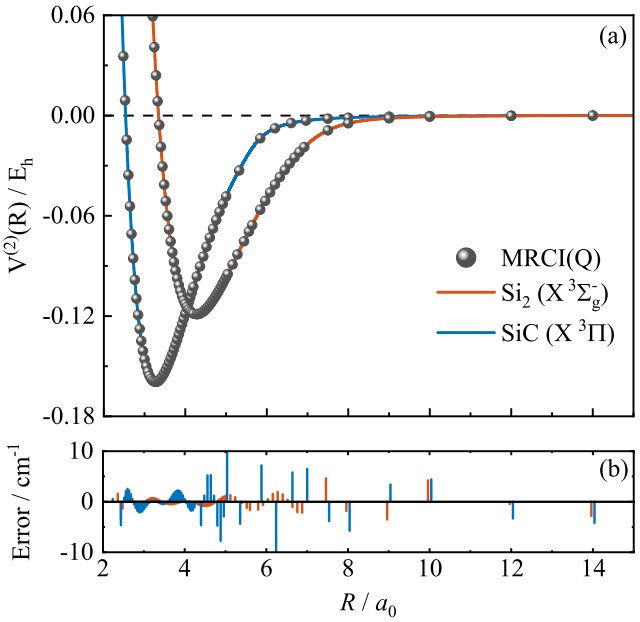

Figure 1. (a) The PECs of $Si_2(X\,^3\Sigma_g^-)$ and $SiC(X\,^3\Pi)$. The solid lines are the PECs fitted by equation (8), and the close circles are the *ab initio* energy points. (b) The deviations between fitted and *ab initio* potential energies.

Table 1. Equilibrium geometries (R_e), dissociation energies (D_e), and harmonic vibrational frequencies (ω_e) of $Si_2(X\,^3\Sigma_g^-)$ and $SiC(X\,^3\Pi)$.

	R_e/a_0	D_e /eV	ω_e /cm^{-1}
$Si_2(X\,^3\Sigma_g^-)$			
This work[a]	4.27	3.237	506.11
Exp.[b]	4.24	3.209	510.98
Exp.[c]	4.24	3.250	509 ± 10
Theor.[d]	4.24	–	512.75
Theor.[e]	4.12	3.253	516.30
$SiC(X\,^3\Pi)$			
This work[a]	3.27	4.339	951.40
Exp.[f]	3.25	–	965.16
Exp.[g]	–	4.467	–
Theor.[h]	3.25	–	965.79
Theor.[i]	3.25	4.470	967.21

Note.[a] Fitted by *ab initio* energies using the CHIPR function of equation (8). [b] Huber & Herzberg (1979). [c] Kitsopoulos et al. (1991). [d] Shi et al. (2011). [e] Dixon et al. (2000). [f] Butenhoff & Rohlfing (1991). [g] Drowart, De Maria & Inghram (1958). [h] Shi et al. (2012). [i] Xing, Shi & Sun (2019).

4 FEATURES OF THE PES

The potential energy curves (PECs) of $Si_2(X\,^3\Sigma_g^-)$ and $SiC(X\,^3\Pi)$ are respectively obtained by fitting 89 and 70 *ab initio* MRCI(Q) potential energy points using equation (8). The fitting parameters M in equation (4) and L in equation (8) were chosen to be 4 and 8 for each two-body term, respectively. As shown in Fig. 1(a), the obtained CHIPR PECs reproduce accurately the calculated *ab initio* potential energies with rmsds of 1.3 and 3.4 cm^{-1} for $Si_2(X\,^3\Sigma_g^-)$ and $SiC(X\,^3\Pi)$, respectively. The deviations between *ab initio* potential energies and fitted energies are presented in Fig. 1(b) and are within $\pm 10\,cm^{-1}$. The equilibrium geometries (R_e), dissociation energies (D_e), and harmonic vibrational frequencies (ω_e) of $Si_2(X\,^3\Sigma_g^-)$ and $SiC(X\,^3\Pi)$ are shown in Table 1.

Table 2. The stratified rmsd of $Si_2C(X\ ^1A_1)$ CHIPR PES.

Energy[a]	N^b	Max error[c]	Rmsd[d]	N>rmsd[e]
10	408	1.19	0.180	22
20	485	1.32	0.233	43
30	531	1.46	0.287	63
40	586	1.69	0.394	92
50	630	1.69	0.450	115
60	667	1.90	0.487	134
70	704	2.16	0.523	151
80	763	2.27	0.560	173
90	855	2.27	0.602	222
100	1003	2.27	0.654	269
200	3149	2.28	0.710	842
300	3633	2.28	0.733	984
500	3850	2.28	0.753	1055
1000	4080	2.28	0.767	1105

Note.[a] Energy in kcal mol^{-1}. [b] The number of calculated potential energy points up to the indicated energy range. [c] Maximum error (in kcal mol^{-1}) up to the indicated energy range. [d] Energy in kcal mol^{-1}. [e] The number of calculated points with an energy deviation larger than the rmsd.

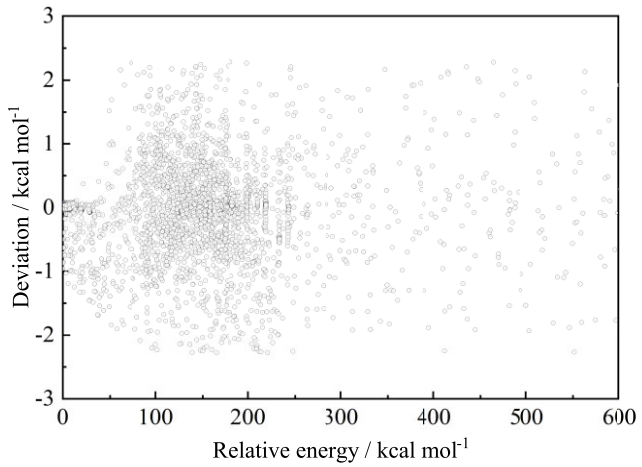

Figure 2. A scatter plot of deviation between fitted and calculated *ab initio* energies as a function of the total energy. In the *x*-axis, the zero is set relative to the GM of Si_2C.

The partial and accumulated rmsd of the CHIPR PES are listed in Table 2. A total of 4080 *ab initio* points were utilized in the CHIPR 4.0 program, covering an energy range up to 1000 kcal mol^{-1} above the GM of $Si_2C(X\ ^1A_1)$. In addition, Fig. 2 shows the distribution of deviations between the fitted and *ab initio* data. The total rmsd of the fitting PES is 0.769 kcal mol^{-1}, showing the high fitting precision of the present PES.

Table 3 displays the properties of the stationary points on the PES of $Si_2C(X\ ^1A_1)$, including the bond lengths for SiSi (R_1) and SiC (R_2, R_3), potential energies (E) relative to the $C(^3P) + Si(^3P) + Si(^3P)$ asymptote, and harmonic frequencies ω_i ($i = 1$ for symmetrical stretching, 2 for bending stretching and 3 for antisymmetric stretching). The predicted bond lengths and harmonic frequencies of the GM on the CHIPR PES show good agreement with previous theoretical and experimental results (Grev & Schaefer 1985; Presilla-Márquez & Graham 1991; Barone et al. 1992; McCarthy et al. 2015; Reilly et al. 2015; Koput 2017; Witsch et al. 2019)

The major features of the $Si_2C(X\ ^1A_1)$ PES are illustrated in Figs 3 and 4. Fig. 3(a) shows a 2D PES for the bending angle of the ∠[Si–C–Si] fixed at 113.25°. As can be seen, the GM is the unique $C_{\infty v}$ symmetric conformation located at $R_1 = 5.378\ a_0$ and $R_2 = R_3 = 3.220\ a_0$. As shown in Table 3, the predicted harmonic frequencies are in good agreement with the theoretical results calculated at the CCSD(T)/cc-pV7Z level (Koput 2017) and the experimental values (McCarthy et al. 2015; Witsch et al. 2019). Figs 3(b) and (c) illustrate the contour plots for linear [Si–C–Si] and [C–Si–Si] geometries, respectively. As shown in Fig. 3(b) and Table 3, the linear $D_{\infty h}$ transition state (TS) locates at $R_2 = 3.210\ a_0$, with a well depth of –0.3951 E_h relative to the $C(^3P) + Si(^3P) + Si(^3P)$ asymptote and 1.44 kcal mol^{-1} relative to the GM structure. Earlier experimental (Reilly et al. 2015) $D_{\infty h}$ TS has a barrier of 2.24 kcal mol^{-1} relative to the GM structure, which is closer to our predicted value given in Table 3. The attributions of the $D_{\infty h}$ TS are similar to those from our geometry optimization (OPTG) result at the MRCI(Q)/AVQZ level and previous theoretical calculations (Grev & Schaefer 1985; Barone et al. 1992). Fig. 3(c) and Table 3 show that the linear $C_{\infty v}$ TS has a bond length of $R_1 = 4.156\ a_0$ and $R_2 = 3.359\ a_0$. Fig. 3(d) illustrates the plot for the insertion of the C atom into the Si_2 molecule along the C_{2v} symmetry and shows little difference between the energies of the GM and $D_{\infty h}$ TS structures. The exchanging of two Si atoms makes Figs 3(a) and (d) show perfect symmetry.

Figs 4(a) and (b) illustrate the contour plots for the C and Si atoms moving around the SiSi and SiC molecules, respectively. The bond lengths of the SiSi and SiC molecules are fixed at their equilibrium geometries, where $R_{SiSi} = 4.11\ a_0$ and $R_{SiC} = 3.27\ a_0$. Figs 3 and 4 show smooth and reasonable behaviours in the whole space, warranting good performance of the present PES.

To better view all major topographical features, the relaxed triangular plot (Varandas 1987) is displayed in Fig. 5, which uses the scaled hyperspherical coordinates ($\beta* = \beta/Q$, $\gamma* = \gamma/Q$):

$$\begin{pmatrix} Q \\ \beta \\ \gamma \end{pmatrix} = \begin{pmatrix} 1 & 1 & 1 \\ 0 & \sqrt{3} & -\sqrt{3} \\ 2 & -1 & -1 \end{pmatrix} \begin{pmatrix} R_1^2 \\ R_2^2 \\ R_3^2 \end{pmatrix} \tag{10}$$

As shown in Fig. 5, all stationary points of the ground-state $Si_2C(X\ ^1A_1)$ are visible and well reproduced. Based on Fig. 5, the connection of each stationary point can be established more comprehensively.

5 REACTION DYNAMIC CALCULATIONS

Based on the ground state CHIPR PES of $Si_2C(X\ ^1A_1)$, the dynamics of the $C(^3P) + Si_2(X\ ^3\Sigma_g^-) \rightarrow Si(^3P) + SiC(X\ ^3\Pi)$ reaction were investigated by using the QCT (Hase et al. 1996) and time-dependent wave packet (TDWP) methods.

The QCT simulations were carried out following the earlier work (Li et al. 2022). We ran the calculations with 10^5 trajectories at each collision energy for ensuring convergence and accuracy. To warrant the conservation of the total energy within 10^{-4} E_h or smaller, a time-step of 0.1 fs is utilized in the integration of Hamilton's motion equations. The distance between the C atom and the Si_2 molecule was initially separated by 15 Å. The ICS of $C + Si_2$ ($v = 0$–3, $j = 0$) → Si + SiC were calculated by (Li, Caridade & Varandas 2014)

$$\sigma_r(v, j) = \pi b_{\max}^2 \frac{N_r}{N}, \tag{11}$$

where N is the total number of the trajectories, N_r is the number of the reactive trajectories, and b_{max} is the maximum impact parameter which is optimized by trial and error. The thermal rate coefficient is

Table 3. The characteristics of the stationary points on the CHIPR PES of $Si_2C(X\,^1A_1)$.

Structure	R_1/a_0	R_2/a_0	R_3/a_0	E^a	ω_1 /cm^{-1}	ω_2 /cm^{-1}	ω_3/ cm^{-1}
GM							
This work	5.378	3.220	3.220	−0.3974	850	150	1205
Theor.[b]	5.529	3.186	3.186	-	823	94	1429
Theor.[c]	5.392	3.209	3.209	-	833[c]	140[c]	1203[c]
Exp.[d]	-	-	-	-	840	172	1188
Exp.[e,f]	5.392[e]	3.199[e]	3.199[e]	-	832[f]	142[f]	1202[f]
Exp.[g]	-	-	-	-	851	150	1223
$D_{\infty h}$ transition state							
This work	6.420	3.210	3.210	−0.3951	706	102*i*	1141
AVQZ[h]	6.422	3.211	3.211	−0.3950	571	84*i*	1380
Theor.[b]	6.312	3.156	3.156	-	641	75*i*	1511
Theor.[i]	6.426	3.213	3.213	-	569	84*i*	1394
$C_{\infty v}$ transition state							
This work	4.156	3.359	7.515	−0.2563	790	528	115*i*
AVQZ[h]	4.180	3.361	7.541	−0.2568	910	463	107*i*

Note.[a] Energy (in E_h) relative to the $C(^3P) + Si(^3P) + Si(^3P)$ asymptote. [b] (Grev & Schaefer 1985). [c] Theorical fundamental frequencies reported in Koput (2017). [d] (Presilla-Márquez & Graham 1991). [e] Experimental equilibrium parameters reported in McCarthy et al. (2015). [f] Experimental fundamental frequencies reported in Reilly et al. (2015). [g] (Witsch et al. 2019). [h] Results from the geometry optimization. [i] (Barone et al. 1992).

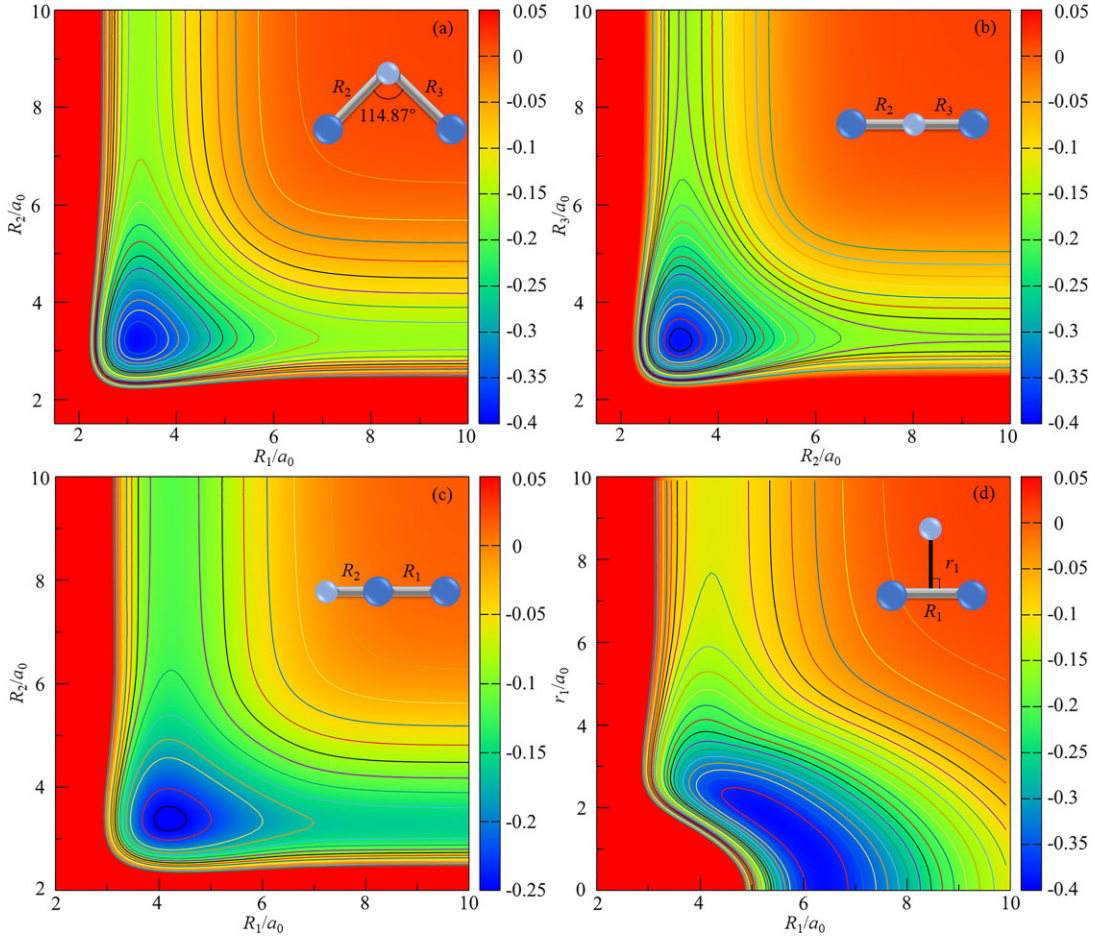

Figure 3. The contour plots (a) at the fixed included angle $\angle$[SiCSi] $= 114.87^\circ$, (b) for the linear [Si–C–Si], (c) for the linear [C–Si–Si], and (d) for the C_{2v} insertion of the C atom into the Si_2 fragment. Contours are equally spaced by 0.015 E_h for panel (b) and 0.02 E_h for the others, starting at –0.4 E_h for panels (a), (b), and (d), and –0.25 E_h for panel (c).

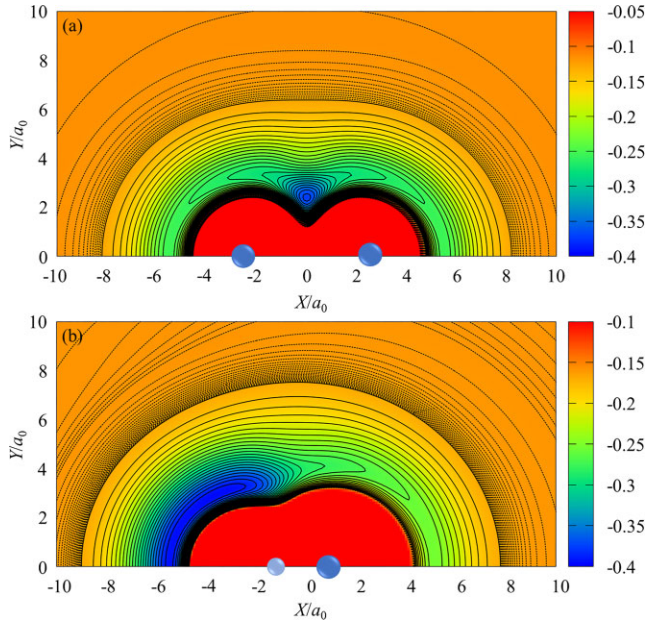

Figure 4. (a) The contour plot for C moving around the Si_2 fragment (R_{SiSi} = 4.11 a_0) which lies along the x-axis with the centre of the Si_2 bond being fixed at the origin. Contours are equally spaced by 0.01 E_h, starting at –0.4 Eh. Dashed areas are the contours equally spaced by 0.001 E_h. (b) The contour plot for Si moving around the SiC fragment (R_{SiC} = 3.27 a_0) lies along the x-axis with the centre of the mass being fixed at the origin. Contours are equally spaced by 0.01 E_h, starting at –0.4 E_h. Dashed areas are the contours equally spaced by 0.0001 E_h.

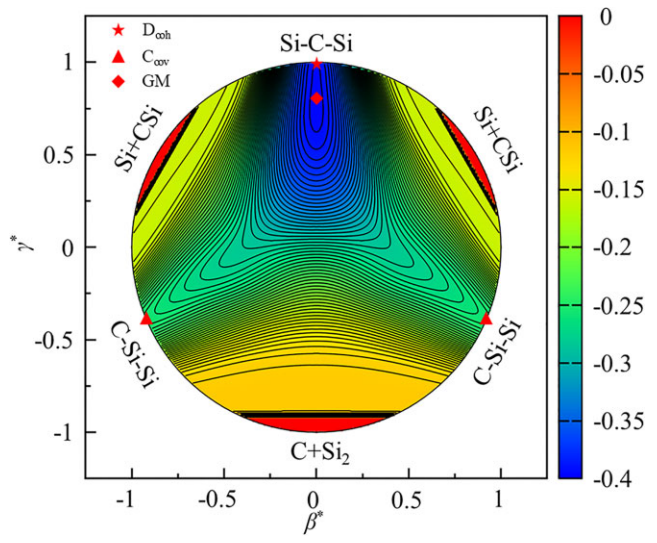

Figure 5. The relaxed triangular contour plot for the $Si_2C(X\ ^1A_1)$ PES in hyperspherical coordinates. Contours start at –0.4 E_h and are equally spaced by 0.005 E_h.

calculated by

$$k(T) = g_e(T)\left(\frac{8k_BT}{\pi\mu_{C+SiSi}}\right)^{1/2}\pi b_{max}^2\frac{N_r}{N}, \tag{12}$$

where k_B is the Boltzmann constant, μ_{C+SiSi} is the reduced mass of the reactants, and $g_e(T)$ is the electronic degeneracy factor (Graff & Wagner 1990), which is defined as

$$g_e(T) = q_{Si_2C}(T)q^{-1}_{C(^3P)}(T)q^{-1}_{Si_2}(T), \tag{13}$$

where the degeneracy of the ground state $Si_2C(X\ ^1A_1)$ is 1, and the electronic degeneracy factors which account for the fine structures of the $Si_2(X\ ^3\Sigma_g^-)$ and $C(^3P)$ assume the expression (Graff & Wagner 1990)

$$q_{Si_2}(T) = 3 \tag{14}$$

$$q_{C(^3P)}(T) = 1 + 3\exp(-23.62/T) + 5\exp(-62.46/T) \tag{15}$$

The TDWP method utilized here was widely used in previous works (Zhang & Zhang 1993; Zhang et al. 2003, 2004; Li et al. 2022). The Hamiltonian of the $C + Si_2(X\ ^3\Sigma_g^-)$ system in the reactants' Jacobi coordinates takes this form:

$$H = -\frac{\hbar^2}{2\mu_R}\frac{\partial^2}{\partial R^2} + \frac{(\hat{J}-\hat{j})^2}{2\mu_R R^2} + \frac{\hat{j}^2}{2\mu_r r^2} + V(R,r) + h(r), \tag{16}$$

where R is the distance between the C atom and the centre-of-mass of Si_2, r indicates the diatomic distance of Si_2, μ_R is the reduced mass between C and Si_2, μ_r is the mass of Si_2, $\hat{J}$ and $\hat{j}$ are the total angular momentum, and the rotational angular momentum of Si_2, respectively. $V(R, r)$ is the CHIPR PES for the $Si_2C(X\ ^1A_1)$ system. The diatomic reference Hamiltonian $h(r)$ can be written as

$$h(r) = -\frac{\hbar^2}{2\mu_r}\frac{\partial^2}{\partial r^2} + V(r), \tag{17}$$

where $V(r)$ is the potential function of Si_2.

After providing the initial wave packet, it was propagated on the PES using the following split-operator scheme:

$$\psi^{JM\epsilon}(\vec{R},\vec{r},t+\Delta) = e^{-iH_0\Delta/2}e^{-iU\Delta}e^{-iH_0\Delta/2}\psi(\vec{R},\vec{r},t), \tag{18}$$

where ψ is the wave packet, H_0 is the reference Hamiltonian, and U is the effective potential operator, H_0 and U are given by

$$H_0 = -\frac{\hbar^2}{2\mu_R}\frac{\partial^2}{\partial R^2} + h(r) \tag{19}$$

$$U = \frac{(\hat{J}-\hat{j})^2}{2\mu_R R^2} + \frac{\hat{j}^2}{2\mu_r r^2} + V(\hat{R},\hat{r}) \tag{20}$$

After a sufficiently long period of propagation, the reaction probability can be extracted from the final wave packet using the standard TD reactive flux method:

$$P^J_{v_0,j_0,k_0}(E) = \frac{\hbar}{\mu_r}\mathrm{Im}\left[\psi(E)\left|\delta(r-r_0)\frac{\partial}{\partial r}\right|\psi(E)\right], \tag{21}$$

where v_0, j_0, and k_0 (the projection quantum number of j_0) are the initial state quantum numbers and r_0 represents the position where the flux analysis is carried out. The total reaction ICS and temperature-dependent rate constant are then calculated by

$$\sigma_{v_0j_0k_0}(E) = \frac{\pi}{k^2}\sum_J(2J+1)P^J_{v_0j_0k_0}(E) \tag{22}$$

$$\sigma_{v_0j_0}(E) = \frac{1}{2j_0+1}\sum_{\kappa_0}\sigma_{v_0j_0k_0}(E) \tag{23}$$

$$k_{v_0j_0}(T) = \sqrt{\frac{8k_BT}{\pi\mu_R}}(k_BT)^{-2}\int_0^\infty E\sigma_{v_0j_0}(E)\exp\left(-\frac{E}{k_BT}\right)\mathrm{d}E, \tag{24}$$

where k_B is the Boltzmann constant and k is the wavenumber corresponding to the initial state at a fixed collision energy E.

Fig. 6 shows the insertion reaction path for the $C(^3P) + Si_2(X\ ^3\Sigma_g^-)$ $\rightarrow Si(^3P) + SiC(X\ ^3\Pi)$ reaction and the energies of related stationary

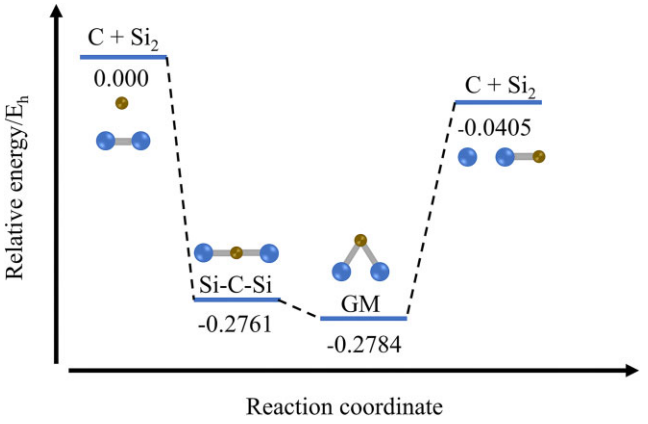

Figure 6. The energy diagram for the insertion reaction pathway and relative stationary points of $C(^3P) + Si_2(X\ ^3\Sigma_g^-) \rightarrow Si(^3P) + SiC(X\ ^3\Pi)$ reaction. Energies in E_h are given relative to the $C(^3P) + Si_2(X\ ^3\Sigma_g^-)$ asymptote.

Table 4. Parameters used in the TDWP calculations[a].

Parameters	Value
Scattering coordinate (R) range	0.01 – 20
Number of grid points in R	400
Diatomic coordinate (r) range	2.5 – 20
Number of grid points in r	240
Absorption region length in R (r)	3.0 (3.0)
Absorption strength in R (r)	0.03 (0.03)
Centre of initial wave packet R_0	16
Initial translational energy (eV)	0.5
Time-step for propagation	10
Total propagation time	150 000

Note.[a] All parameters are given in atomic units, except for the numbers of quantities or indicated otherwise.

points on this novel PES. Without activation barriers, the insertion of the C atom may approach along the mid-perpendicular of Si_2, leading directly to the GM. The GM structure is subsequently converted to the reaction intermediate, namely linear $D_{\infty h}$ TS, with R_2 and R_3 increasing and ∠[Si–C–Si] opening progressively, as shown in Fig. 3(d). Finally, the $D_{\infty h}$ TS dissociates and converts into the $Si(^3P)$ and $SiC(X\ ^3\Pi)$ products. As Fig. 6 shows, the $C(^3P) + Si_2(X\ ^3\Sigma_g^-) \rightarrow Si(^3P) + SiC(X\ ^3\Pi)$ reaction is a highly exoergic reaction (0.0405 E_h), so we can conclude that this reaction can play an important role in the formation of gas-phase SiC and solid SiC dust.

For barrierless exoergic reactions with deep wells, the quantum dynamics calculations can be expensive (Lin et al. 2008; Bulut et al. 2011; Rao et al. 2013; Goswami et al. 2022). Here we only consider the dynamics of the $C + Si_2\ (v = 0, j = 0) \rightarrow Si + SiC$ reaction. Through many tests for the convergence of the total angular momentum $J = 0$, the obtained parameters are listed in Table 4.

The total ICSs for the $C(^3P) + Si_2(X\ ^3\Sigma_g^-; v = 0–3, j = 0) \rightarrow Si(^3P) + SiC(X\ ^3\Pi)$ reactions as a function of the collision energy of 0.1 – 1.0 eV are displayed in Fig. 7. As shown, the ICSs obtained from the QCT and QM calculations have the same varying trend. Since there is no barrier on the minimum energy path, the ICSs obtained from both the QCT and QM calculations decrease rapidly with the increase of the collision energy and gradually level off at high collision energies. Meanwhile, the oscillation characteristics of the QM results are shown over the whole range of collision energy considered here, and the amplitude of oscillation decreases with the

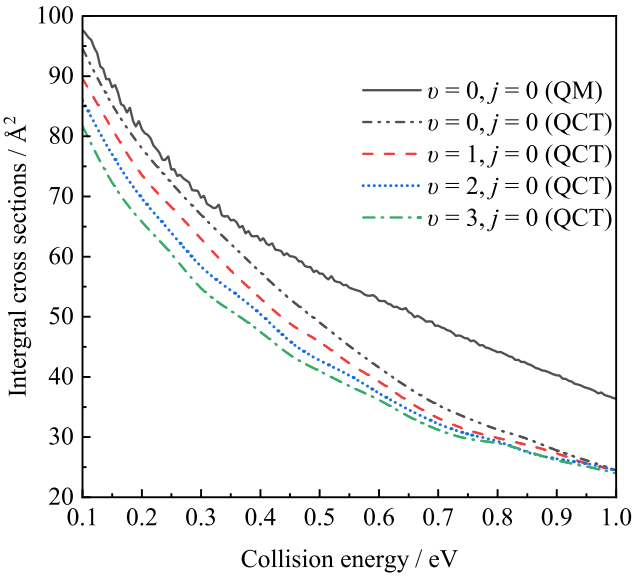

Figure 7. The ICSs (Å^2) for the $C(^3P) + Si_2(X\ ^3\Sigma_g^-; v = 0–3, j = 0)$ reaction as a function of the collision energy for several vibrational quantum numbers $v = 0, 1, 2, 3$ with the rotational quantum number of $j = 0$.

increase of the collision energy, which are similar to previous studies (Sundaram, Manivannan & Padmanaban 2017; Gao et al. 2019). Moreover, the quantum ICSs for $v = 0, j = 0$ are typically larger than the QCT counterparts, showing the importance of quantum effects in this reaction.

As shown in Fig. 7, the vibrational excitation of the diatomic reactant Si_2 has a significantly negative effect on the ICSs. When $j = 0$, all ICSs decrease with the increase of the vibrational quantum numbers v in the collision energy range from 0.1 to 0.9 eV. This phenomenon might indicate that the vibrational excitations of the reactant Si_2 restrain the reaction and reduces the ICSs at this collision energy range. With the further increase of the collision energy, the ICSs tend to be identical.

Fig. 8 shows the rate constants versus temperatures from 150 to 3000 K for $C(^3P) + Si_2(X\ ^3\Sigma_g^-) \rightarrow Si(^3P) + SiC(X\ ^3\Pi)$ obtained by QCT and QM methods. As shown, the rate constants obtained by QCT and QM calculations have the same trend which elevates gradually with the increasing temperature and then reach a plateau at high temperatures. Because the quantum tunneling effect and the zero-point energy leakage problem are not considered, the QCT results are systematically lower than the QM values. Then, the rate constants obtained by QCT and QM calculations are fitted using the three-parameter kooij function (Laidler 1996), which is defined as

$$k(T) = A\left(\frac{T}{300}\right)^m e^{-\beta_k/T}. \quad (25)$$

For QCT, A, m, and β_k are 4.51789 × 10^{-11} cm^3 s^{-1}, 0.08535, and 89.76252 K, respectively. For QM, the parameters A, m, and β_k have the values of 4.64706 × 10^{-11} cm^3 s^{-1}, 0.12203, and 26.91122 K, respectively.

6 CONCLUSIONS

For the first time, we have reported a global CHIPR PES of the ground state $Si_2C(X\ ^1A_1)$ system based on a total of 4080 *ab initio* points calculated at the MRCI(Q) level with AV(Q + d)Z and AVQZ basis set. The equilibrium geometries, dissociation energies, and harmonic vibrational frequencies of $Si_2(X\ ^3\Sigma_g^-)$ and $SiC(X\ ^3\Pi)$ obtained from

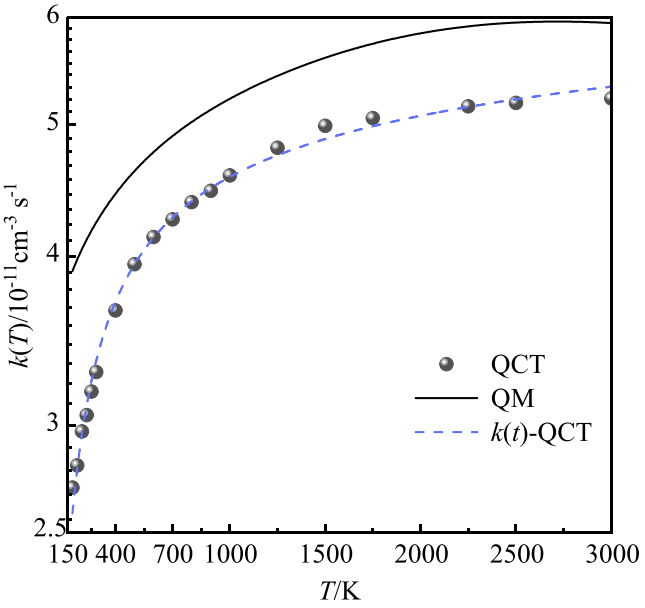

Figure 8. The rate constants (k) as a function of the temperature (T) for the $C(^3P) + Si_2(X\ ^3\Sigma_g^-)$ reaction. The solid grey circles correspond to the results obtained from QCT calculations. The black solid line corresponds to the results obtained from QM calculations. The blue dashed line corresponds to the QCT results fitted using the kooij function.

the CHIPR PECs show good agreement with the experimental values. Topographical characteristics including the equilibrium geometries, energies, and vibrational frequencies of the stationary points obtained from the CHIPR PES are discussed in detail and compared well with available theoretical and experimental values. Based on the CHIPR PES, ICSs, and rate constants for the $C(^3P) + Si_2(X\ ^3\Sigma_g^-) \rightarrow Si(^3P) + SiC(X\ ^3\Pi)$ reaction are calculated using the QCT and QM methods. For the lack of available experimental and theoretical values, our results are made an analogy with the other barrierless exothermic reactions and show reasonable order of magnitude and variation tendency. The ICSs for the reaction show that the vibrational excitation has a significantly negative effect on reactivity.

The obtained CHIPR PES for ground state $Si_2C(X\ ^1A_1)$ shows reasonable and smooth behaviour over the whole configuration space and can be used to construct PES for larger molecular systems, such as the $Si_2C + H_2$ system (Cabrera-González et al. 2023). Our computed ICSs and rate constants can be useful for modelling chemical evolution towards AGB carbon star IRC+10216.

ACKNOWLEDGEMENTS

This work was financed by the National Natural Science Foundation of China (Grant number 52106098), the Natural Science Foundation of Shandong Province (Grant number ZR2021QE021), the China Post-doctoral Science Foundation (2021M701977), the Post-doctoral Innovation Project of Shandong Province, and the Post-doctoral Applied Research Project of Qingdao City. The scientific calculations in this paper have been done on the HPC Cloud Platform of Shandong University.

DATA AVAILABILITY

The FORTRAN code for CHIPR PES are available at MNRAS online.

REFERENCES

Barone V., Jensen P., Minichino C., 1992, J. Mol. Spect., 154, 252
Bolton E. E., DeLeeuw B. J., Fowler J. E., Grev R. S., Schaefer H. F., III, 1992, J. Chem. Phys., 97, 5586
Bulut N., Roncero O., Jorfi M., Honvault P., 2011, J. Chem. Phys., 135, 104307
Butenhoff T. J., Rohlfing E. A., 1991, J. Chem. Phys., 95, 3939
Cabrera-González L. D., Páez-Hernández D., Stoecklin T., Denis-Alpizar O., 2023, Phys. Chem. Chem. Phys., 25, 4542
Cernicharo J., Gottlieb C., Guelin M., Thaddeus P., Vrtilek J., 1989, ApJ, 341, L25
Cernicharo J. et al., 2015, ApJ, 806, L3
Cernicharo J. et al., 2018, A&A, 618, 4
Chen G., Qin Z., Li J., Liu L., 2022, Phys. Chem. Chem. Phys., 24, 19371
Cordiner M., Millar T., 2009, ApJ, 697, L68
Diercksen G. H., Grüner N., Oddershede J., Sabin J. R., 1985, Chem. Phys. Lett., 117, 29
Ding Z., Qin Z., Liu L., 2023, Phys. Fluids, 35, 027127
Dixon D. A., Feller D., Peterson K. A., Gole J. L., 2000, J. Phys. Chem. A, 104, 2326
Drowart J., De Maria G., Inghram M. G., 1958, J. Chem. Phys., 29, 1015
Dunning T. H. Jr, 1989, J. Chem. Phys., 90, 1007
Frenklach M., Carmer C., Feigelson E., 1989, Nature, 339, 196
Gabriel W., Chambaud G., Rosmus P., Spielfiedel A., Feautrier N., 1992, ApJ, 398, L706
Gao F., Zhang L., Zhao W., Meng Q., Song Y., 2019, J. Chem. Phys., 150, 224304
Gobrecht D., Cristallo S., Piersanti L., Bromley S. T., 2017, ApJ, 840, L117
Goswami S., Veliz J. C. S. V., Upadhyay M., Bemish R. J., Meuwly M., 2022, Phys. Chem. Chem. Phys., 24, 23309
Graff M., Wagner A., 1990, J. Chem. Phys., 92, 2423
Grev R. S., Schaefer H. F., III, 1985, J. Chem. Phys., 82, 4126
Hase W. et al., 1996, Google Scholar Quantum Chemistry Program. Exchange Bull, 16, 43
Huber K.-P., Herzberg G., 1979, Molecular spectra and molecular structure: IV. Constants of diatomic molecules. D. Van Nostrand, New York
Kafafi Z. H., Hauge R. H., Fredin L., Margrave J. L., 1983, J. Phys. Chem., 87, 797
Kitsopoulos a., Chick C., Zhao Y., Neumark D., 1991, J. Chem. Phys., 95, 1441
Knowles P. J., Werner H.-J., 1985, Chem. Phys. Lett., 115, 259
Knowles P. J., Werner H.-J., 1988, Chem. Phys. Lett., 145, 514
Koput J., 2017, J. Mol. Spect., 342, 83
Laidler K. J., 1996, Pure Appl. Chem., 68, 149
Largo-Cabrerizo A., Flores J., 1988, Chem. Phys. Lett., 145, 128
Li J., Caridade P. J., Varandas A. J., 2014, J. Phys. Chem. A, 118, 1277
Li X., Qin Z., Li J., Liu L., 2022, Phys. Chem. Chem. Phys., 24, 26564
Lin S. Y., Guo H., Honvault P., Xu C., Xie D., 2008, J. Chem. Phys., 128, 014303
Mauron N., Huggins P., 2000, A&A, 359, 707
McCarthy M. C., Baraban J. H., Changala P. B., Stanton J. F., Martin-Drumel M.-A., Thorwirth S., Gottlieb C. A., Reilly N. J., 2015, J. Phys. Chem. Lett., 6, 2107
McCarthy M. C., Gottlieb C. A., Cernicharo J., 2019, J. Mol. Spect., 356, 7
McElroy D., Walsh C., Markwick A., Cordiner M., Smith K., Millar T., 2013, A&A, 550, 36
Murrell J. N., Carter S., Farantos S C., Huxley P., Varandas A. J., 1984, Molecular potential energy functions. Wiley, Chichester
Pellarin M. et al., 1999, J. Chem. Phys., 110, 6927
Prasad S., Huntress W., Jr, 1980, ApJS, 43, 1
Presilla-Márquez J., Graham W., 1991, J. Chem. Phys., 95, 5612
Rao T. R., Goswami S., Mahapatra S., Bussery-Honvault B., Honvault P., 2013, J. Chem. Phys., 138, 094318
Reilly N. J., Changala P. B., Baraban J. H., Kokkin D. L., Stanton J. F., McCarthy M. C., 2015, J. Chem. Phys., 142, 231101
Rittby C., 1991, J. Chem. Phys., 95, 5609
Rocha C. M., Varandas A. J., 2020, Comput. Phys. Commun., 247, 106913

Rocha C. M., Varandas A. J., 2021, Comput. Phys. Commun., 258, 107556
Rocha C. M., Linnartz H., Varandas A. J., 2022, J. Chem. Phys., 157, 104301
Sabin J. R., Oddershede J., Diercksen G. H., Grüner N. E., 1986, J. Chem. Phys., 84, 354
Schmude R. W., Gingerich K. A., 1997, J. Phys. Chem. A, 101, 2610
Sharma M., Chandra S., 2022, Astrophysics, 65, 266
Shi D.-h., Liu H., Sun J.-f., Zhu Z.-l., Liu Y.-f., 2011, J. Quant. Spect. Rad. Trans., 112, 2567
Shi D., Xing W., Sun J., Zhu Z., 2012, Eur. Phys. J. D, 66, 1
Smith I. W., Herbst E., Chang Q., 2004, MNRAS, 350, 323
So S. P., 1985, J. Chem. Soc., Faraday Trans. 2: Mol. Chem. Phys., 81, 139
Spielfiedel A., Carter S., Feautrier N., Chambaud G., Rosmus P., 1996, J. Phys. Chem., 100, 10055
Steglich M., Maier J. P., 2015, ApJ, 801, L119
Sundaram P., Manivannan V., Padmanaban R., 2017, Phys. Chem. Chem. Phys., 19, 20172
Varandas A., 1987, Chem. Phys. Lett., 138, 455
Varandas A., 2013, J. Chem. Phys., 138, 054120
Varandas A. J., 2014, in Han K., Chu T., eds, Reaction Rate Constant Computations: Theories and Applications, Chapt. 17. Royal Society of Chemistry, Cambridge, p. 408
Varandas A., 2018a, Phys. Chem. Chem. Phys., 20, 22084
Varandas A. J., 2018b, Ann. Rev. Phys. Chem., 69, 177
Verhaegen G., Stafford F., Drowart J., 1964, J. Chem. Phys., 40, 1622
Weltner W., Jr., McLeod D., Jr., 1964, J. Chem. Phys., 41, 235
Werner H.-J., Knowles P. J., 1985, J. Chem. Phys., 82, 5053
Werner H.-J., Knowles P. J., 1988, J. Chem. Phys., 89, 5803
Werner H.-J. et al., 2015, MOLPRO, version 2015.1, a package of ab initio programs, see http://www.molpro.net
Werner H.-J., et al., 2020, J. Chem. Phys., 152, 144107
Witsch D., Lutter V., Breier A. A., Yamada K. M., Fuchs G. W., Gauss J., Giesen T. F., 2019, J. Phys. Chem. A, 123, 4168
Xing W., Shi D., Sun J., 2019, J. Quant. Spect. Rad. Trans., 227, 86
Zhang D. H., Zhang J. Z., 1993, J. Chem. Phys., 99, 6624
Zhang Y., Xie T.-X., Han K.-L., Zhang J. Z., 2003, J. Chem. Phys., 119, 12921
Zhang Y., Xie T.-X., Han K.-L., Zhang J. Z., 2004, J. Chem. Phys., 120, 6000
Zhu A., et al., 2022, The Lancet Regional Health-Western Pacific, 20, 100372

SUPPORTING INFORMATION

Supplementary data are available at *MNRAS* online.

Supplemental material.zip

Please note: Oxford University Press is not responsible for the content or functionality of any supporting materials supplied by the authors. Any queries (other than missing material) should be directed to the corresponding author for the article.

This paper has been typeset from a TEX/LATEX file prepared by the author.